Mechanics and stability of vesicles and droplets in confined spaces

Eduard Benet and Franck J. Vernerey

Phys. Rev. E **94**, 062613 — Published 29 December 2016

DOI: 10.1103/PhysRevE.94.062613

Mechanics and stability of vesicles and droplets in confined spaces

Eduard Benet and Franck J. Vernerey
University of Colorado at Boulder, department of mechanical engineering
(Dated: December 1, 2016)

The permeation and trapping of soft colloidal particles in the confined space of porous media is of critical importance in cell migration studies, design of drug delivery vehicles and colloid separation devices. Our current understanding of these processes is however limited by the lack of quantitative models that can relate how the elasticity, size and adhesion properties of the vesicle/pore complex affects colloid transport. We address this shortcoming by introducing a semi-analytical model that predicts the equilibrium shapes of a soft vesicle driven by pressure in a narrow pore. Using this approach, the problem is recast in terms of pressure and energy diagrams that characterize the vesicle stability and permeation pressures in different conditions. We particularly show that the critical permeation pressure for a vesicle arises from a compromise between the critical entry pressure and exit pressure, both of which are sensitive to geometrical features, mechanics and adhesion. We further find that these results can be leveraged to rationally design micro-fluidic devices and diodes that can help characterize, select and separate colloids based on physical properties.

Keywords: vesicles; colloids; microfluidics; fluidic diodes; stability

I. INTRODUCTION

The separation and trapping of micron and nano-sized colloidal particles by porous media has been and still is the object of a number of studies with important outcomes in a variety of disciplines. In chemical engineering and the food industry [1], efficient filtration processes heavily depend on both the design of membranes targeting colloidal particles [2], and their treatment on the formation of cakes [3, 4]. In medicine, effective strategies to capture circulating tumor cells (CTC's) in the blood stream could enable the detection of certain forms of cancer at an early stage and improve treatment with patient specific therapies [5, 6]. To address those needs, researchers and engineers have developed a large spectrum of microfluidics [7], membranes [8] and experimental techniques [9] aimed to capture and separate colloidal particles, most of them using particle size as the segregation criterion.

Separation based on the physical properties of particles, such as deformability and adhesion/wetting are however less common. In spite of our limited understanding of these processes, recent techniques have been devised based on the apparent correlation between colloid properties (surface tension, particle elasticity) and their ability to permeate through narrow pores. These techniques could indeed be critical in the separation and trapping of particles with similar sizes but different properties, which include for instance, CTC's and leucocytes [10]. In this context, efforts have focused on microfluidic devices that possess gradual variations in pore size [11] such that particles of distinct mechanical properties can be separated [12] or trapped [13] depending on their position in the device. Recently, studies by Sarioglu [14] and McFaul [15] have further shown that pore shape can be used as a design criterion for particle separation. These studied indeed showed that anisotropic pores, or "microfluidic diodes" [16] could act as valves allowing deformable particles to travel in only one direction. One key lesson from these studies is that deformability, in addition to size, should be considered in the design of filtration membranes and micro-fluidic devices. But particle separation is not the sole application of these new technologies; the critical pressure and deformation of a particle in a nano-pore (or channel) may also be used to learn about its mechanical response. For instance, as early as 1989, Evans *et al.* [17] proposed to use a micropipette aspiration test to determine the surface tension, membrane elasticity, and/or viscosity of soft colloids. This technique is now considered as a standard [18] for quantifying the mechanics of a variety of particles including cells [19] and vesicles [20]. Variations of this strategies have also been proposed, including for instance, the use of conical microchannels to determine the elastic properties of bacteria based on their equilibrium position under a pressure gradient [21].

A number of theoretical studies have been proposed to understand and guide experimental efforts, but to date, have exclusively targeted the critical pressure that is necessary for a particle to enter a pore. These include the derivation of analytical expressions relating surface tension and elasticity to the entry of a vesicle in a cylindrical channels mimicking a micropipette [18] or anopore membranes [22]. Extension to non-circular openings were also proposed analytically by Bruus *et al.* [23] for more complex pore shapes. However, when more complex pore or vesicle shapes are considered, solutions must be derived numerically as discussed by Leong et al. [24] in the context of vesicle properties and Zhang et al. [25] in the context of pore shapes. Besides deformability, the physical interactions between a pore and a particle, and particularly their mutual adhesion, are also known to be an important factor to the permeation problem [26] but surprisingly, studies on this topic are scarce in the literature. Indeed, while the physics of adhesion between a vesicle and a substrate is widely known, it was not until the work of Fournier et al. [27] that it was applied to the permeation of a vesicle through axisymmetric pores of varying cross-sections (both cylindrical and conical). Using an enhanced version of the Laplace law accounting for both the bending stiffness and the adhesion of a lipid membrane, the authors derived relationships between the pressure applied along the channel and the shape acquired by a vesicle. The relationship between entry pressure, permeation pressure and the deformability, size and adhesion energy of a colloidal particle in an arbitrary pore is however still poorly understood.

In this work, we propose to fill this gap by adopting a theoretical/numerical approach that considers the interactions of a vesicle characterized by its surface tension, size and adhesion energy with an axisymmetric pore of arbitrary cross-section. We particularly aim to understand the interplay between pore geometry and particle adhesion on the physics of vesicle permeation, which includes the phenomena of entry, exit and trapping within pores. Results are presented in terms of pressure and energy diagrams that enable the visualization of the various mechanical instabilities undergone by a vesicle traveling through a pore and how they are affected by pore aperture, curvature, and asymmetry. We further show that the exit pressure, in addition to entry pressure, is a key feature for the permeation of moderately adhesive particles.

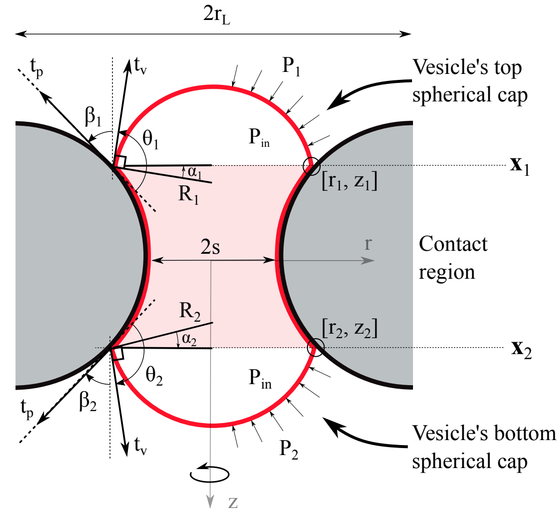

FIG. 1. Scheme of a vesicle in equilibrium due to a pressure difference $P_1 - P_2$ in an axisymmetric pore with minimum aperture radius s. The vesicle is divided in three parts by the two contact lines $\mathbf{x}_1 = [r_1, z_1]$ and $\mathbf{x}_2 = [r_2, z_2]$: two spherical caps with radii R_1 and R_2 and the contact region in between. The spherical caps meet the pore at the contact line i with an angle of θ, which is defined by the tangent at the pore $\mathbf{t}_p$, and the vesicle $\mathbf{t}_v$. The volume of each cap is defined by their radii inner angle α_i between the horizontal and the radius at the detachment point. These magnitudes are all related by the angle that the pore tangent makes with the vertical β_i, defined positive counterclockwise in the top cap and clockwise in the bottom one.

II. EQUILIBRIUM MECHANICS OF A VESICLE IN A PORE

We concentrate here on a class of deformable particles, or vesicles, whose structure can be represented by an inner fluid surrounded by a thin viscous membrane with surface tension γ. Such a system constitutes a generic model for a variety of living and non-living particles including cells, liposomes, droplets or microbubbles. Note that although this approach is exact for immiscible fluid droplets, it is usually not the case for particles coated by a thin shell (lipids for instance). In this case, areal extension can arise from two different phenomena: (a) a stretch of thermal fluctuations associated with a rise in surface tension [28] as seen in liposomes [29]. (b) The unfolding of excess area stored in the membrane in the form of wrinkles [17]. This has been observed in the deformation of neutrophils wherein the change in tension was negligible [30]. We further note that in the case where a vesicle is not spherical, the approach should incorporate the effect of the lipid shell bending rigidity κ [31, 32]. Thus, in general Helfrich et al. [33] have shown that a vesicle at equilibrium possesses a pressure drop across its interface ΔP_I which depends on the membrane properties as:

$$\Delta P_I = 2\gamma H - 2\kappa\left(2H(H^2 - K) - \Delta_s H\right) \quad (1)$$

where H and K are the mean and gaussian curvatures on the membrane respectively, and Δ_s is the surface Laplacian operator. To fully solve the immersed membrane problem usually requires a sophisticated numerical approach such as that proposed by Foucard et al. [34]. For simplicity, the present approach considers the case of apparently spherical vesicles that possess small surface fluctuations that can stretch under force. In this case, as pointed out by Fournier and Galatola [27], Eq. (1) degenerates to the classical Laplace law $\Delta P_I = 2\gamma H$ when the minimum radius of curvature verifies $R \gg \sqrt{\kappa/\gamma}$. Thus, for a majority of apparently spherical vesicles whose surface tension is on the order of $10^{-3} N/m$ [35] and bending resistance $\kappa \approx 10^{-19} Nm$ [36] Laplace law holds for radii larger than a critical value $R_c = 0.1\mu m$. For microbubbles however, the surface tension and bending modulus are on the order of $10^{-2} N/m$ [37] and $10^{-19} Nm$ [38] respectively, and the Laplace approximation is restricted to smaller critical radii, near $R_c = 0.01\mu m$. The case of cells is however more complex since the presence of the cortex gives them a viscoelastic behavior [39] both in stretch and bending. Hence, this approach is only valid in cases where the deformation is purely due to the membrane unfolding as observed in the micropipette aspiration of neutrophils [40].

Let us consider an incompressible vesicle of radius $R > R_c$ trapped in an axisymmetric pore whose smallest aperture is $s < R$ (Fig. 1). At equilibrium, the deformation of this vesicle depends on the pressure drop across the pore $\Delta P = P_2 - P_1$, the surface tension of the vesicle γ and its contact angle with the pore θ ($\frac{\pi}{2} < \theta < \pi$ for partially wetting vesicles [41]). Contact angles below $\pi/2$ would imply a preference for the vesicle to wet the pore by splitting, and/or sticking to the side of the pore surface [42]. This situation is fundamentally different from the objective of our study and is therefore not considered. For small capillary numbers [18] and in the absence of body forces, the morphology of the vesicle can be divided into three sections: two free spherical caps whose curvatures ρ_1 and ρ_2 are determined by Laplace law $\rho_i = (P_i - P_{in})/2\gamma$ with P_{in} the internal vesicle pressure, and a confined section (shaded in Fig. 1) whose geometry is restricted by the pore shape. Mathematically, these regions are characterized by the coordinates of two contact lines $\mathbf{x_1} = [r_1, z_1]$ and $\mathbf{x_2} = [r_2, z_2]$ and the pore shape parametrization $\mathbf{x} = (r(z), z)$, where (r, z) are cylindrical coordinates about a system whose origin is at the center of the pore. The global equilibrium of the vesicle can be easily derived by taking the difference between ρ_2 and ρ_1 in order to obtain:

$$\Delta P = 2\gamma \left(\rho_2 - \rho_1\right). \tag{2}$$

Note that this expression is only valid for equilibrium or quasistatic systems in which the inner vesicle pressure is homogeneous and there is no fluid flow around the pore. A dynamic approach would require to solve the Navier-Stokes equations coupled with the membrane governing equations [43]. By simple geometrical relations, one can show that the cap curvatures can be related to the pore geometry by $\rho_i = -\cos(\theta + \beta_i)/r_i$ where r_i and $\beta_i = \arctan(r'(z_i))$ are the radii and the signed tangent angle (with $r' = dr/dz$) of each contact lines (Fig. 1). Using the Young-Dupre relation [41], the contact angle can further be related to the adhesion energy Γ between the vesicle and the pore by $cos(\theta) = -\Gamma/\gamma - 1$, allowing us to express the cap curvatures in terms of the surface energy as:

$$\rho_i = \frac{1}{\gamma r_i}\left[\gamma \cos\beta_i + \Gamma\left(\cos\beta_i + \sin\beta_i\sqrt{-1 - 2\frac{\gamma}{\Gamma}}\right)\right] \tag{3}$$

This relation, together with Eq. 2 can be used to compute the pressure drop across a vesicle in a pore, as long as one knows the position of the contact lines $\mathbf{x_1}$ and $\mathbf{x_2}$. It can be useful, for instance, to characterize the tendency of a vesicle to enter a pore by measuring its sudden pressure drop ΔP as it first makes contact with the pore surface. At this point, the two contact lines are confounded (i.e. $r_1 = r_2$ and $\beta_1 = -\beta_2$) and we are left with the term $\Delta P = 4\sin(\beta_1)\frac{\Gamma}{r_1}\sqrt{-1 - 2\frac{\gamma}{\Gamma}}$ which measures the *suction pressure* that drives a vesicle into the pore. A simple observation of this equation show that this pressure increases with adhesion energy Γ and pore orientation angle β_1 but decreases with the contact line radius r_1.

It can also be seen that, taking $\beta_1 = \frac{\pi}{2}$, $\beta_2 = 0$ and $r_2 = s$, (3) directly yields the formula proposed by Fournier and Galatola [27] for the pressure ΔP describing the entry of a vesicle in a cylindrical micropipette of radius s:

$$\Delta P = 2\gamma\left(\frac{1}{s} - \frac{1}{R_1} + \frac{\Gamma}{\gamma s}\right). \tag{4}$$

Again, we clearly see here how the adhesion energy triggers a suction pressure via the term $\Gamma/\gamma s$, that was neglected in the original work of Evans *et al.* [17]. While Eq. 3 is useful for a variety of theoretical investigations, it is not sufficient to compute the positions of the contact lines $\mathbf{x_1}$ and $\mathbf{x_2}$. To close our formulation, we need to enforce the volume conservation of the vesicle during the permeation process. Considering a spherical vesicle of radius R, this implies $4\pi R^3/3 = \sum V_i^c + V^t$ where V_i^c is the volume of the spherical caps ($i = 1, 2$) and V^t is the volume of the section of the vesicle confined in the pore throat. The former can conveniently be expressed in terms of angles α_i made between the radius of the vesicle at the point of contact and the horizontal axis (Fig. 1) as $V_i^c = \pi r(z_i)^3 h(\alpha_i)/3$ with $h(\alpha_i) = (2 + 3\sin(\alpha_i) - \sin^3(\alpha_i))/\cos^3\alpha_i$. Further noticing that $\rho_i r_i = \cos\alpha_i$, the complete system of equations describing the equilibrium of an incompressible vesicle confined in a pore is comprised of Eq. 2 and the volume conservation equation in the form:

$$2\gamma\left(\frac{\cos\alpha_2}{r(z_2)} - \frac{\cos\alpha_1}{r(z_2)}\right) = \Delta P \tag{5}$$

$$\frac{\pi}{3}\sum_{i=1}^{2}\left[r(z_i)^3 h(\alpha_i)\right] + \int_{V_c} dV = \frac{4}{3}\pi R_v^3 \tag{6}$$

with $\alpha_i = \theta + \arctan(r'(z_i)) - \pi$. This nonlinear system admits the coordinates z_i of the two contact lines as solution (when this solution exists), given a pressure drop ΔP across the pore.

For convenience and ease of analysis, it is preferable to non-dimensionalize the above equations. For this, note that the above system has the general form $g = \Delta P - f(\gamma, s, \theta, R, \mathbf{x}) = 0$ where the parameters in f describe the physical properties of the vesicle-pore complex. Scaling forces and lengths by γ and s (the pore aperture), respectively, the Buckingham π theorem states that our problem can be cast in the form $\Delta P^* = \frac{\Delta P \cdot s}{2\gamma} = \tilde{f}\left(\theta, \frac{R}{s}, \frac{\mathbf{x}}{s}\right)$. In other words, we define a normalized vesicle radius $R^* = R/s$ and pore coordinate $z^* = z/s$ such that:

$$\Delta P = \frac{2\gamma}{s} f\left(\theta, R^*, z^*\right). \tag{7}$$

Implicitly, this relation states that the permeation pressure depends on vesicle deformability, which we measure here as the pressure difference across its surface. Indeed, a larger surface tension will increase this pressure difference, making vesicles appear less deformable and exhibit more resistance to pore permeation. On the contrary, a larger pore size reduces the permeation pressure by increasing the length scale of the system. A larger curvature indeed yield a lower pressure within the vesicle, and hence a lower resistance to deformation.

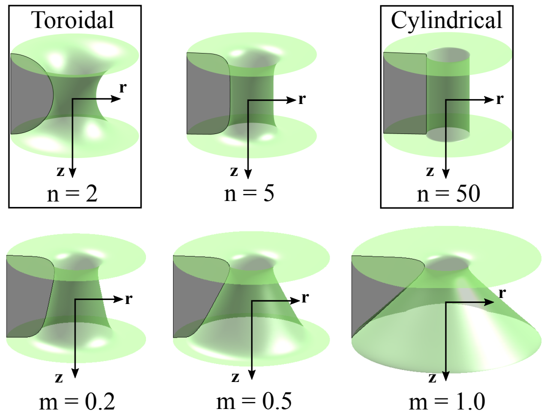

FIG. 2. 3D representation of the axisymmetric pore. On the top three figures, the value of m is kept constant at 0 while we vary the sharpness parameter n. On the bottom figure n is constant and equal to 5 while m is varied.

III. ANALYSIS OF VESICLE INSTABILITY AND CRITICAL PERMEATION PRESSURE

Numerous experimental observations show that vesicle deformation and permeation across a pore are largely dependent on both pore geometry [44] and vesicle adhesion [4]. We aim here to closely investigate these relationships by concentrating on a restricted, yet ubiquitous, set of pore morphologies found in microfluidic devices [45], micropipette aspiration studies [46], filtration membranes [47] and particle trapping devices [15]. The generic axisymmetric pore is described by a tapered hyperelliptical profile with semi-major and semi-minor axes of length a and b, a shape factor n that controls the pore curvature and a slope factor m that controls its asymmetry. The parametrization is written:

$$r(z) = a\left(1 + \frac{m}{b}z\right)\left(\left(1 - \left|\frac{z}{b}\right|\right)^n\right)^{\frac{1}{n}} - r_L, \qquad (8)$$

where $2r_L$ is the exterior diameter of the pore (Fig. 1). As shown in Fig. 2, the shape of the pore ranges from a cylindrical channel of height $2b$ for $n \to \infty$, to a toroidal pore with an ellipsoidal section of axis a, b when $n = 2$. The slope factor further introduces an asymmetry to the pore such that $m = 0$ exhibits a symmetrical top-bottom shape, while more pronounced conical shapes are obtained as the magnitude of m increases. (8) can be used into the system of (5)-(6) to obtain an explicit form of the governing equations and a numerical solution for a variety of pore-vesicle system (details are provided in appendix A).

Equilibrium diagrams. The equilibrium states of a soft vesicle confined in a pore can be visualized by the pressure diagram, showing the position of the center of mass of the vesicle in terms of the pressure drop ΔP across the pore. Fig. 3a-b shows such diagrams for a normalized radius $R^* = 1.5$, adhesion energy $\Gamma = 0$ and toroidal and cylindrical pore geometries. It can be seen that for symmetric pores ($m = 0$) and non-wetting vesicles (solid lines), the diagram possesses three distinct regions (ascending-descending-ascending), delimited in order by the maximum and the minimum values of the pressure drop ΔP. The first region starts when the vesicle is tangent to the pore in its underformed configuration (point A_1), which corresponds to a zero pressure drop. As the pressure increases, the vesicle enter the pore following the branch $A_1 - C_1$ until it reaches the maximum pressure at C_1. In a pressure controlled system, this point yields to an instability where the vesicle, under an infinitesimal pressure increment, would dramatically leave the pore space by rapidly transforming its stored elastic energy into kinetic energy (Forward motion in Fig. 3a). This behavior is typically observed in the micropipette aspiration of neutrophils and the values of the critical pressure have been well estimated using a similar approach [40, 48]. In a displacement driven system, however, the motion of the vesicle towards the pore center A_3 (region 2) would require a decrease in pressure until it reaches point C_2, and eventually A_2 as it exists the pore. For backward motion (the vesicle starts from the bootom of the pore), the first contact occurs in A_2 and the vesicle encounters its instability at C_2, both of which are analogous to A_1 and C_1. For a cylindrical pore, the pressure diagram displays similar trends with two notable differences: (1) the branches $(A_1 - C_1)$ and $(A_2 - C_2)$ are steeper owing to the fact that a sharper pore opening requires a larger vesicle deformation, and (2) the flat region around A_3 corresponds to a situation where the vesicle is free to slide along a cylindrical channel without pressure variations.

The nature of the pressure curve is reminiscent of the equilibrium diagram of “ball on a hill” that first requires energy to reach the top, but that restitutes this potential energy as it loses elevation. Following this analogy, we take an energetic approach wherein the stored mechanical energy in the vesicle is expressed as the difference ΔE in surface energy between the deformed and undeformed vesicle configurations. For an axisymmetric vesicle, this is expressed by:

$$\Delta E = \gamma\left(\sum S_i - S_0 - 2\pi\int_{z_2}^{z_1} r(z)\cos\theta(z)dz\right), \qquad (9)$$

where $S_0 = 4\pi R^2$ is the initial surface area of the vesicle and $S_i = 2\pi r(z_i)^2(1 - \sin\alpha_i)/\cos(\alpha_i)^2$ are the surface areas of top and bottom spherical caps. We observe here that for non-wetting vesicles ($\theta = \pi$), this energy is proportional to an increase in the vesicle's surface area due to deformation. The normalized energy landscapes ($\Delta E^* = \Delta E/\gamma S_0$) shown in Fig. 3c-d clearly show that as the vesicle moves forward and deforms, energy must be provided until it reaches the center point $z = 0$, while energy is restituted afterwards. We also note that the branch $A_1 - C_1$ is stable (concave region), the branch $(C_1 - A_3)$ is unstable (convex region) and the inflection point C_1 denotes the onset of instability. We finally observe that point A_3 corresponds to a metastable equi-

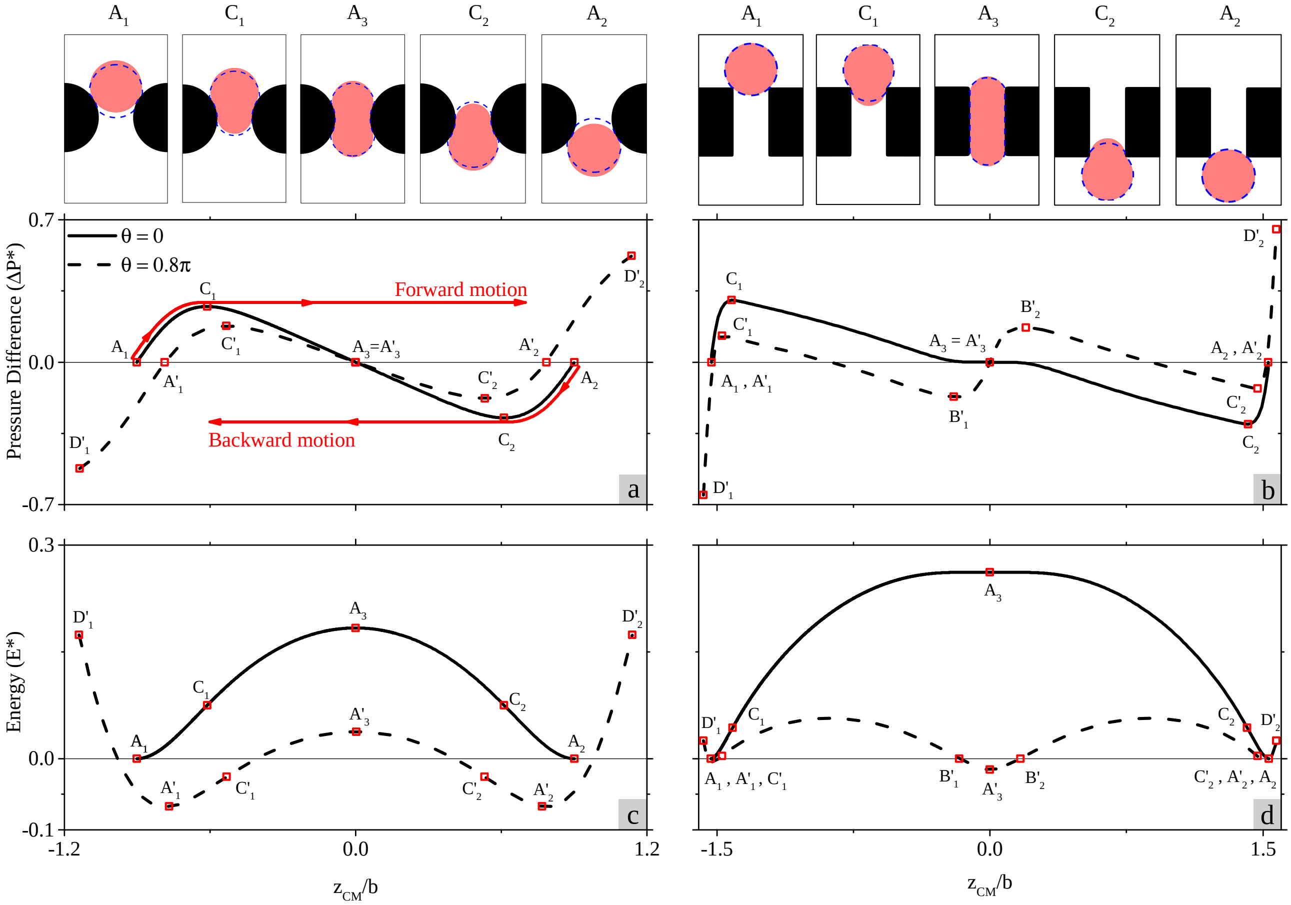

FIG. 3. Equilibrium and energy diagrams for two vesicles of radius $R^* = 1.5$ and adhesion energies $\Gamma = 0$ (solid lines) and $\Gamma = -0.19$ (dashed lines) in a toroidal ($n = 2$) and a cylindrical pore ($n = 50$) with $m = 0$ and $a = b = 2s$. (a) and (b) show the variation of the equilibrium pressure with the relative position of the center of mass z_{CM}/b for both vesicles in each respective pore. A_i mark the locations of the points at 0 pressure, C_i the maximum entry pressure and B_i, D_i the local and absolute maximum suction pressure. The section of the most relevant positions is show in the top insets. The red lines show the path followed by a pressure driven vesicle in both directions. Graphics (c) and (d) show the variation of the energy with the relative position of the center of mass z_{CM}/b and the corresponding position of each point.

librium with maximum mechanical energy (largest vesicle deformation); any small deviation in pressure would therefore push the vesicle towards A_1 or A_2. It can also be seen that for a cylindrical pore ($n = 50$) the energy is constant around A_3 since no additional force has to be provided to deform the vesicle in the cylindrical section of the pore. Additionally, these energy diagrams provide important information regarding the direction of motion of the vesicle. In the absence of an external pressure, a vesicle will move towards the closest minimum energy point until it reaches an equilibrium position. The dynamics of motion involves complex processes such as internal fluid flow [18], or/and the appearance of a lubrication layer [49] between the vesicle and the pore, whose study is beyond the scope of this paper.

The role of adhesion. Adhesive pore-vesicle complexes display very different pressure and energy landscapes compared to their non-wetting counterparts. This effect, shown in Fig.3 with dashed-lines for an adhesion energy $\Gamma/\gamma = -0.19$, is two-fold: (a) The pore exerts a suction pressure $\Delta P_{suct} < 0$ as the vesicle first touches the pore (point D'_1) and (b) the system displays several equilibrium positions whose number and stability strongly depend on the pore shape. In particular, for both toroidal and cylindrical geometries, we find that when a vesicle becomes in close proximity the entry point, it will naturally enters the throat to reach the equilibrium position A'_1 (or A'_2 for backward entry). If a positive pressure is applied, the vesicle follows a stable branch until it reaches the local pressure maximum at C'_1 similar to a non-wetting vesicle studied above. By contrast, a pressure increment at this point would not push the vesicle out of the pore but rather move it to the next equilibrium branch, $C'_2 - A'_2$ for the toroid or $A'_3 - B'_2$ for the cylinder. A much larger pressure ΔP_{suct} needs to be applied to completely remove the vesicle from the pore at D'_2. It can therefore be concluded that for a partially wetting vesicle in a toroidal pore, the critical permeation pres-

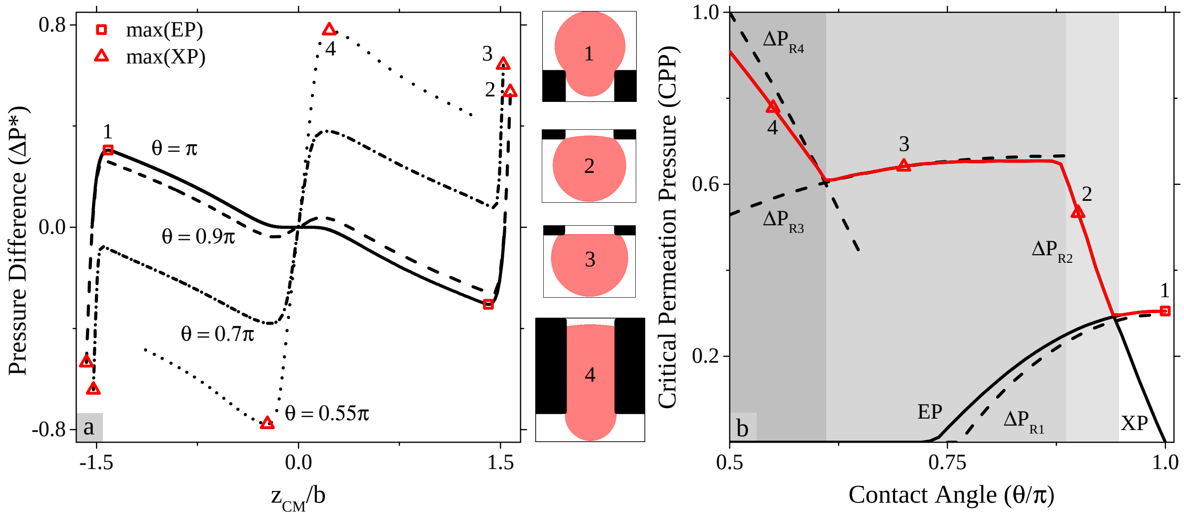

FIG. 4. (a). Equilibrium diagrams of four vesicles of the same relative size $R^* = 1.5$, but with different adhesion energies corresponding to $\theta = 0.55\pi$, 0.7π, 0.9π and π, in a pore with geometrical properties $n = 50$, $a = b = 2s$ and $m = 0$. The position of maximum entry pressure (EP) has been labeled with a square while the exit pressure (XP) has been labeled with a triangle. (b). The critical permeation pressure, the maximum of (EP) and (XP), is plotted versus the adhesion energy (θ) for the permeation of a vesicle with relative size $R^* = 1.5$ in a cylindrical pore with $n = 50$, $a = b = 2s$ and $m = 0$. The graphic displays four different regimes depending on the permeation mechanism of the vesicle, which have been differentiated by the vertical shading. In each of them, there is an inset figure showing an example of the position of the vesicle when the critical pressure was achieved. The dotted lines show the analytical expressions derived for this problem in its range of validity.

sure is the maximum of $\Delta P(C_1')$ and $\Delta P(D_2')$. Interestingly, when the pore changes from toroidal to cylindrical, point A_3' changes from an unstable to a stable position. In other words, during its permeation, the vesicle may "jump" from one stable position to another (A_1'- A_3' - A_2') until it is allowed to leave the pore when the maximum pressure at D_2 is applied. The permeation pressure is now determined by the competition between $\Delta P(C_1')$, $\Delta P(D_1')$ and $\Delta P(B_2')$.

The critical permeation pressure (CPP). A number of experimental and theoretical studies [18, 19, 22, 25, 50] have focused on evaluating the maximum pressure drop (CPP) for a vesicle to go through (i.e. enter and exit) a pore. The distinction between pore entry pressure (EP) and CPP is however not explicit in these studies, and the effects of pore throat geometry (rather than opening) and adhesion are often neglected. Here, we aim to show that these effects are in fact critical to the physics of vesicle permeation and/or trapping and that it is possible to tune the pore geometry and chemistry to achieve desired behaviors. We have seen in Fig. 3a-b that two quantities become particularly important when studying the CPP: the maximum entry pressure (EP) at C_1 (or C_2 for backward motion), and the maximum exit pressure (XP) at D_2 (or B_2) that typically increases with adhesion energy. Generally, the CPP can therefore be defined as the maximum between the EP and the XP; Fig. 4a illustrates this relation for a cylindrical pore ($n = 50$), where the maximum of the equilibrium diagram (CPP) shifts from the EP to XP as the contact angle is decreased from π to $\pi/2$. Fig. 4b further shows that the relationship between CPP and adhesion is not trivial and it is dictated by the pore-vesicle interactions either during the entry or the exit of the pore. Four main regimes are observed, each of them associated to one of the four types of equilibrium diagrams depicted in Fig. 4a: for small adhesion energies (contact angle near $\theta = \pi$), the critical pressure is dictated by the EP (Fig. 4 inset 1) which, for a perfectly cylindrical channel, can be expressed in terms of the contact angle as [22]:

$$\Delta P^*_{R1} = \cos\theta \left[\left(\frac{2 - 3\cos\theta + \cos^3\theta}{\sin\theta + \sin^3\theta - 4R^{*3}\cos^3\theta - 2} \right)^{\frac{1}{3}} - 1 \right], \tag{10}$$

and which occurs at C_1, highlighted with a square in Fig. 4. As the adhesion energy increases, the equilibrium diagrams shift to the point where the pressure at C_1 coincides with D_2 in Fig. 4a, the mechanism of vesicle permeation becomes *capillary driven*, i.e. $CPP = XP$ (red triangles in Fig. 4). The next three regimes are therefore dominated by XP, rather than the entry pressure. In the second regime, for low to intermediate adhesion energies, the model shows that the vesicle exits the pore via a peculiar mechanism in which both contact lines merge, yielding no room for pore-vesicle contact. This corresponds to the maximum of an equilibrium diagram such as the one with $\theta = 0.9\pi$ in Fig. 4a, where the vesicle shape is described by two coexistent spherical caps of different radii that are barely in contact with the pore as shown in Fig.4, inset 2. In this regime, the pressure coincides with the expression previously calculated for the case when $\mathbf{x_1} = \mathbf{x_2}$:

$$\Delta P^*_{R2} = -2\frac{\sin(\beta)\sin\theta}{r^*(z)}, \tag{11}$$

until the mechanism drastically switches to regime 3. Indeed, for intermediate values of the adhesion energy, the model shows that the loss of vesicle equilibrium occurs through a flattening of its upper cap while remaining in contact with the lower portion of the pore (Fig.4, inset 3). As the top curvature vanishes, the force balance (Eq. 2) on the vesicle can no longer be satisfied, forcing the particle out of the pore space. In this situation, the critical pressure can be analytically approximated by considering a single spherical cap whose contact line radius is larger than the pore aperture:

$$\Delta P^*_{R3} = \frac{1}{R^*}\left((1-\cos\theta)(\sin^2\theta + 1 - \cos\theta)/4\right)^{\frac{1}{3}}, \tag{12}$$

This expression (derived in appendix B) agrees reasonably well with our numerical solution at $n = 50$. Note that despite the fact that the associated equilibrium diagram in Fig 4a has its maximum in a very similar position, the CPP evolution is quite different due to a different exit mechanism. Finally, for a contact angle approaching $\pi/2$, yet another exit mechanism is predicted by the model. Here, the adhesive interaction is so strong that the pressure required to exit its stable position at A'_3 (Fig. 4a, point 4), becomes larger than the suction pressure at D'_2. This means that the vesicle is forced out of the pore without settling in its stable position at A'_2. In this case, the CPP can be analytically approximated by (derivation in appendix B):

$$\Delta P^*_{R4} = \sin(\theta) + \cos(\theta). \tag{13}$$

We note here that the small discrepancy between this expression and numerical results observed (region 4 in Fig. 4) is due to the fact that the above solution is based on an opening curvature ($n \to \infty$) while the numerical solution is based on a finite value of the curvature (n).

Asymmetric pores. Asymmetric pores can be designed to enable easy vesicle permeation in one direction but block their entry in the other [51]. For instance, McFaul et al. [52], showed that the critical pressure of cells in conical pores depends their direction, and its value is well estimated by the present model. In Fig. 5a, we show the typical vesicle deformation and the associated pressure diagram for a conical pore whose slope parameter is $m = 0.4$ (other relevant parameters are $n = 50$, $R^* = 1.5$ and $\Gamma/\gamma = -0.05$). A few key observations can be made related to the pore asymmetry. **(a)** the equilibrium diagram is no longer symmetric since the entry and exit mechanisms are different depending on whether a vesicle moves forwards or backwards into the pore. **(b)** Since vesicle entry is almost exclusively driven by the geometry of the pore mouth but not its throat, the pressure diagram is almost unaffected by the pore asymmetry before EP is reached. A similar EP is therefore observed

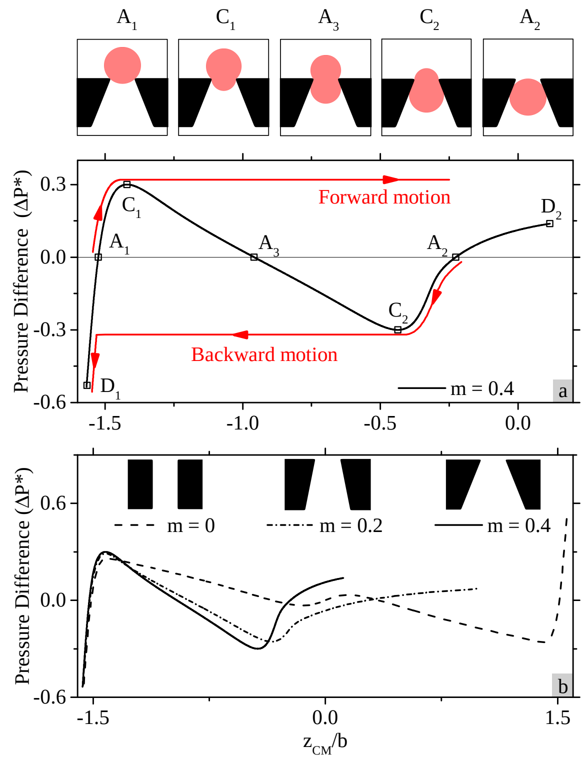

FIG. 5. (a) Equilibrium diagram of a vesicle with radius $R^* = 1.5$ and contact angle $\theta = 0.9\pi$ inside a pore with $m = 0.4$, $a = b = 2s$ and $n = 50$. The relevant positions of the vesicle have been labeled, being A_1, A_2 and A_3 the positions at zero pressure, C_1, C_2 the entry pressure and D_1, D_2 the exit pressure. (b) Equilibrium diagrams for the cases where $m = 0, m = 0.2$ and $m = 0.4$ for the same contact angle to illustrate the effect of pore asymmetry on the curves' evolution

for cylindrical and conical pores with the same entry radius (s) and curvature (or shape factor n) as shown in Fig. 5b. **(c)** The exit pressure (XP) is strongly affected by pore asymmetry. Indeed, for this system, the XP (pressure at D_2) is around 0.1 for a vesicle moving forward, while it is on the order of 0.5 for a vesicle moving in the reverse direction. To understand the consequences of these observations, consider a vesicle undergoing a forward-backward cycle into the pore (Fig. 5a). On its way forward, the vesicle first reaches its equilibrium position at $\Delta P = 0$ before it slowly moves into the pore under increasing pore pressure. The entry instability is reached at point C_1, after which, any additional increase in pressure forces the vesicle out of the pore, since the $XP < EP$. In other words, the forward permeation pressure is $CPP^+ = EP \approx 0.3$ in this system. On its way backwards, the vesicle first settles in its equilibrium position at A_2 before it is forced into the pore under a negative pressure drop. After reaching the entrance instability at C_2, the vesicle jumps into the next equilibrium branch at B_1. It will finally be forced out of the pore if the pressure drop exceeds (in magnitude) the XP at D_1. For backward motion, the critical permeation pressure is therefore $CPP^- = XP \approx 0.5$ in this system. Fig. 5b shows that the pressure diagram, and particularly the region corresponding to the exit mechanism, is very sensitive to the slope of the conical pore. This implies that the geometric design of the pore can be harvested to tune the difference between the CPP for forward and backward motion, a feature that, for instance, is important for designing microfluidic diodes.

IV. VESICLE SEPARATION, TRAPPING AND PROFILING

The design of pores that are capable of targeting specific particles for fractionation, separation and trapping is key to a number of technological applications. We focus here on three important problems in membrane science, vesicle profiling and the design of microfluidic diodes for complex fluids and colloids.

Vesicle separation. In membrane filtration or separation techniques [53], we aim to separate populations of deformable particles using criteria such as size, deformability or adhesion properties. We ask here whether it is possible to design pore geometries, characterized by their aperture size $s/R = 1/R^*$ and curvature (or shape parameter n) in order to achieve very distinct CPPs for two vesicle populations. For this, we first investigate the effect of curvature at a fixed relative vesicle size by varying the pore shape from a toroidal shape ($n = 2$) to a cylindrical shape ($n = 50$) and determined the CPP for a range of contact angles $\pi/2 \leq \theta \leq \pi$ as shown in Fig. 7a. We find that smoother, more rounded pores tend to (a) decrease the CPP for all ranges of adhesion and (b) shift the transitions between different permeation regimes to the left. This trend is particularly true for toroidal pores ($n = 2$) where the mechanism associated to (13) completely disappears. To understand the effect of pore aperture, we performed a similar study by varying R^* at fixed pore curvature $n = 2$ (Fig. 7b). The model shows that pore aperture and vesicle adhesion play two competing roles during the permeation process. For low adhesion, the process is dominated by the EP required to deform the vesicle into the pore; this explains why the CPP increases sharply with vesicle size in this region (right end side of Fig. 7b). By contrast, for larger adhesion, the process becomes dominated by capillary effects (i.e. XP). Interestingly, we find that this pressure decreases with increasing vesicle size (or decreasing aperture) and that this phenomenon yields an inversion of the trends: small apertures yield a smaller CPP. This observation can be understood by looking at the force balance on the vesicle as shown in Fig 6. In the case of high adhesion, the curvature of the inner cap is typically small compared to that of the outer cap (see insets 2-4 in Fig. 4). This implies that vertical forces pulling the vesicle inwards mostly arise from the surface tension in the outer cap. Since capillary forces are proportional to curvature, smaller vesicles (or increasing apertures) tend to display a higher resistance to exit the pore. With these competing mechanisms, we observe that for a toroidal pore, the CPP curves for different vesicle sizes intersect at a value close to $\theta \approx 0.8\pi$. In other words, two vesicles with equal surface tension and adhesion but different sizes can exhibit the same CPP.

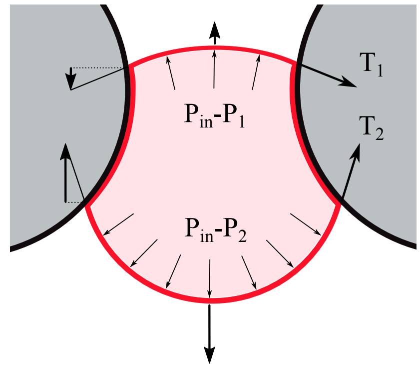

FIG. 6. *Schematic of the forces acting on the vesicle. The resultant from the tension on each cap T_i is directly proportional to its curvature and tangent to the contact point. This surface forces are balanced by the resultant of the pressure difference across the interface $P_{in} - P_i$*

Valuable insights can be gained from the above predictions. For instance, two particles with the same surface tension but different size and adhesion can be separated by properly designing a pore that ensures a very distinct CPP. This strategy can further be optimized by altering the wetting properties of pores with techniques such as electrowetting [26]. In the context of deformability-based particle separation [12, 13, 25], we note that our predictions are for normalized pressure $\Delta P^* = \Delta P s/2\gamma$, implying that pore opening s and surface tension must also be accounted for to distinguish between two particles with different mechanical properties. Dimensional versions of the diagrams presented in Fig. 7 may therefore be preferable for design purposes.

Vesicle profiling. Quantitative observations of particle deformation in narrow pores [21] and micro-pipettes [54] have traditionally been used as a method to indirectly measure their physical properties. We here concentrate on micropipette aspiration for which standard experiments and modeling efforts have focused on cylindrical pipettes with constant cross-sections. Using this technique, a relation between vesicle shape and suction pressure can be measured and used to estimate various properties such as surface tension, elasticity or viscosity [55]. A typical issue, however, is that not all vesicles' equilibrium position entering a micropipette are stable ones [19] and since the aspiration technique is pressure driven, a vesicle only remains stable when the suction pressure is below the EP. We have seen in Fig. 3b that for a cylindrical pore with a sharp corner, the EP is reached at very small vesicle deformation. In other words, this classical design suffers from two major drawbacks: (a)

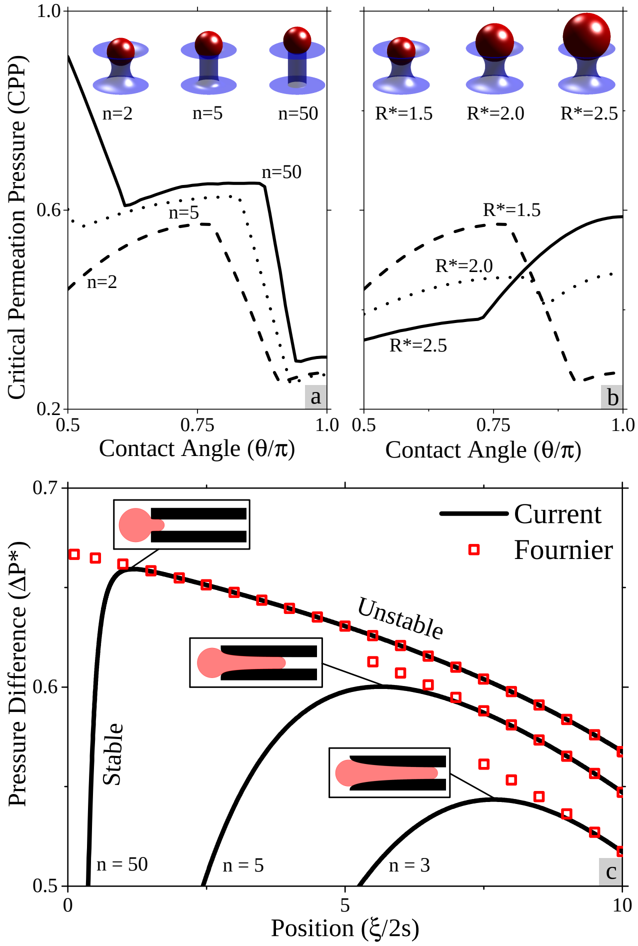

FIG. 7. CPP variation with the contact angle (θ) in (a) three different pore shapes ($n = 2,\ 5,\ 50$) with $a = b = 2s$, $m = 0$ and a vesicle of $R^* = 1.5$, and (b) three different values of the relative vesicle size ($R^* = 1.5,\ 2.0,\ 2.5$) on a toroidal pore ($n = 2$) with $a = b = 2s$ and $m = 0$. For clarity, six insets depict the shape of each pore with the respective vesicle tangent to them. (c) Detail of the equilibrium diagram for three different pores with $a = 2s$, $b = 20s$ and $n = 3,\ 5,\ 50$, for the same vesicle ($R^* = 1.5$, $\Gamma = 0$) and its comparison by the solution proposed by Fournier et al. for the equilibrium pressure in a cylindrical pore. Three insets depict the position of the vesicle at the moment when the EP is achieved. Note that the volume of the axisymmetic vesicle remains constant regardless of its configuration and despite the apparent change in projected areas seen in the figures.

the deformation of the vesicle is highly sensitive to suction pressure, a feature that can affect measurements' accuracy and (b) the vesicle's response can only be surveyed within the range of small deformation, which strongly restricts our ability to fully characterize its mechanical response. A solution to these limitations is suggested in Fig. 3(a) where we found that more rounded pore tend to both postpone the EP and decrease the slope of the pressure-displacement curve. Based on this idea, we show in Fig. 7c the pressure diagram for a cylindrical pipette whose mouth curvature is varied from $n = 50$ (very sharp) to $n = 3$ (very smooth). As expected, we find that decreasing n postpones the onset of instability, decreases the entry pressure and allows to probe the vesicle for a larger range of deformation by making it less sensitive to shape changes. In these regimes, however, we note that the predictions of standard models, such as proposed by Fournier et al. [27] are limited to the unstable branch of the pressure diagram (shown by square symbols on Fig. 7c) and becomes less accurate as n decreases. Semi-analytical approaches, such as that discussed in this paper, therefore would need to be used in combination with new pipette designs (based on smooth mouth opening) to better probe the properties of vesicles and other soft colloidal particles. Note that certain colloidal particles (bacteria and cells for instance) may display more complex mechanical behaviors and remain stable under the classical pipette aspiration tests [48]. In these cases, a more thorough analysis can be performed to identify pipette designs that enable a better characterization of their properties.

Microfluidic diodes The concept of a fluid diode has been long used in microfluidics [16, 56, 57] with applications in biomedical engineering. The separation of particles that exhibit distinct mechanical properties from their surroundings have motivated the design of asymmetric microfluidic devices that can sort soft and rigid particles under oscillatory flow [14, 15, 52]. To examine the role of pore geometry on particle trapping, we propose here to define a measure of trapping efficiency as the difference $[\Delta P_c] = |CPP^+| - |CPP^-|$ between the critical permeation pressure (CPP) as a vesicle moves forward (superscript $+$) and backwards (superscript $-$) through the pore (8a). With this definition, it is clear that the sign of $[\Delta P_c]$ defines the trapping direction: if $[\Delta P_c] > 0$, vesicles are trapped on the top side of the pore (forward diode), while if $[\Delta P_c] < 0$, they are trapped on the bottom (backward diode). Fig. 8a also illustrates the range of pore pressures ($CPP^- \leq \Delta P \leq CPP^+$) for such a diode to operate efficiently; pressures above CPP^+ allow the permeation of vesicles in both directions, while values below CPP^- do not allow particle permeation in any direction. We finally note that symmetric pores studied in the previous section are inefficient at trapping particles since the antisymmetry of the pressure-displacement diagram implies $[\Delta P_c] = 0$.

To investigate the role of pore size, shape and asymmetry on trapping efficiency, we performed a parametric study which consisted of sweeping the space (m, n, R^*) in order to obtain a three-dimensional graphical representation of the dependency $[\Delta P_c]\,(m, n, R^*)$. Results for a non-wetting ($\Gamma = 0$) and an adhering vesicle ($\Gamma = -0.19$) are provided in Fig. 8b and Fig. 8c, respectively. For convenience, we focused here on forward trapping, i.e. our study was restricted to $[\Delta P_c] \geq 0$. Trends in backward trapping can then be deduced by symmetrically inverting the system. The following key observations can be made regarding the trapping of non-wetting particles

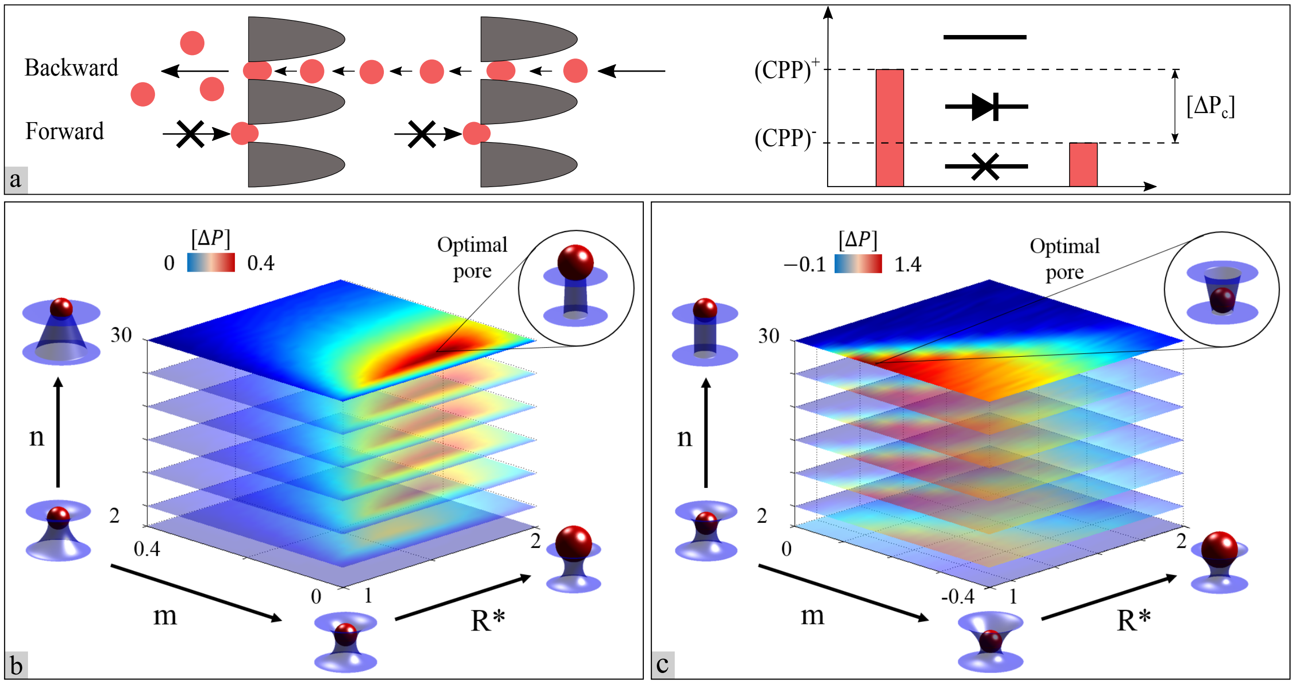

FIG. 8. (a) Scheme of a pore with a funnel shape which has a different critical pressure depending on what direction it is crossed, forward CPP^+ or backward CPP^-. The difference between these two is defined as the trapping efficiency $[\Delta P_c]$ and it indicates how probable is to trap a vesicle using these technique. 4D maps showing the variation on axisymmetric pressure with the relative vesicle radius R^*, the slope m and the shape parameter n are shown for two different vesicles: (a) with $\Gamma = 0$ and (b) with $\Gamma = -0.19$ $(\theta = 0.8\pi)$. The red zones indicate where the axisymmetric pressure is positive and the pore traps particles on top. As opposed to that, the blue zones have a negative pressure asymmetry and vesicles are trapped on the bottom. An circled inset shows the optimal pore and corresponding vesicle in each case.

(Fig. 8b): **(a)** The relationship between pore design and trapping efficiency is nonlinear and exhibits an optimum. **(b)** The optimal design is a slightly tapered (moderate n) conical shape. Indeed, we found that pronounced conical shapes (large m) would lose their "asymmetric power" by providing an overly restrictive pore opening. **(c)** Trapping efficiency is promoted by larger pore curvatures, controlled by the shape parameter n. Figure 8c further shows that the mechanics of asymmetric trapping is strongly affected by adhesion. This observation can be explained by the fact that the CPP is dominated by the XP which involves very different mechanisms than those associated with vesicle entry. In this case, the following pattern emerges: **(a)** The optimal pore is still a cone, but with a more pronounced slope. **(b)** The position of the optimal cone is reversed ($m < 0$) and to catch a vesicle on top we would need the opposite slope, which is not at all intuitive. **(c)** The optimal pore aperture is smaller with adhesion. This is a consequence of the different regimes dominating the XP on each side of the pore. As seen in Fig. 7, small vesicles indeed have larger values of XP which clearly end up dominating the system.

The above analysis could have far reaching potential in the design of membranes, micro-fluidic devices and fluidic diodes for complex fluids. The 3D maps shown in Fig. 8 directly pinpoint the design that offers the highest trapping efficiency for a given particle in order to devise deformability-based systems aimed to separate particles of similar size and adhesion. These maps however need to be complemented by the knowledge of the actual dimensional values of CCP^+, and CPP^- in order to precisely determine the operating pressure corresponding to the device. This can be achieved by reversing the non-dimensional framework.

V. CONCLUSION

In conclusion, we derived a set of nonlinear equations that can describe the permeation of surface tension-dominated adhering vesicles in arbitrary axisymmetric pores. We found that this problem can be studied in terms of pressure and energy landscape that exhibit various equilibrium positions and mechanical instabilities as the vesicles penetrate, travel through and exit from the pore. Interestingly, the maximum pressure for vesicle permeation (CPP) is highly dependent on the mechanisms by which the vesicle interacts with the pore and in particular, their adhesion energy. In particular, model predictions showed that capillary effects produced by vesicle adhesion can play a significant role by creating an suction pressure (XP) that tends to retain the vesicle within the pore. Eventually, vesicles with even slightly different adhesion properties can display significant changes in their permeation abilities. Overall, the results presented in this paper show that one can optimize the design of microfluidic devices, diodes and membranes to specifically target populations of colloids based on their size, surface tension and adhesion properties.

ACKNOWLEDGMENTS

Research reported in this publication was supported by the National Science Foundation under the CAREER award 1350090 and by the National Institute of Arthritis and Musculoskeletal and Skin Diseases of the National Institutes of Health under Award Number 1R01AR065441. The content is solely the responsibility of the authors and does not necessarily represent the official views of the National Institutes of Health.

APPENDIX A: SOLUTION PROCEDURE

Let us consider the problem of a vesicle trapped in an axisymmetric pore spanning in the z coordinate from $-b$ to b and whose geometry is given by (8). The solution is found by solving the system of equations $\boldsymbol{R}$ formed by (Eq. (5) and (6)). However, the solution to this system is not trivial since (1) it is highly non-linear and (2) each value of the pressure drop ΔP leads to multiple solutions for the vesicle position. The latter issue can be simply addressed by enforcing the z-coordinate of one of the contact lines z_i and solve for the corresponding pressure drop and the second detachment point. This operation may be thought of as a *displacement-driven* boundary condition, known to be more stable than a *force-driven condition* for mechanical systems displaying unstable behaviors. The solution of the system is then expressed as the optimization problem $min\,(\mathbf{R}(\mathbf{u}), \mathbf{u} \in \mathcal{F} = \{\mathbf{u} : \mathbf{u}_{LB} \leq \mathbf{u} \leq \mathbf{u}_{UB}\})$, where $\mathbf{u}_{LB}$ and $\mathbf{u}_{UB}$ are the upper and lower bounds of the solution. The non-linearity of the system is primarily caused by the arbitrary definition of the geometry $\mathbf{r}(z)$. This implies that, in general, one can not find a closed form expression for the enclosed volume of the vesicle, and the term $\int_{V_c} dV$ in (6) has to be computed numerically. This has been done by dividing the central volume in N horizontal slices and using a trapezoidal rule:

$$V_c = \int_{z_1}^{z_2} \pi \left(r_L - r(z)\right)^2 dz \tag{14}$$

$$= \sum_{k=1}^{N} \left(\pi (r_L - r_m)^2 \frac{|z_{k+1} - z_k|}{2} \right). \tag{15}$$

where r_m is the average between r_{k+1} and r_k. Hence, since finding a general analytical solution is not possible, we used a trust-region-reflective algorithm with an initial approximation $\mathbf{u}_0 = \{z_i = b, \Delta P = 0\}$ and a tolerance of $||\mathbf{R}|| = 10^{-12}$. This algorithm is widely implemented in multiple platforms and one can for instance use the function *lsqnonlin* built in MATLAB.

APPENDIX B: DERIVATION OF ANALYTICAL SOLUTIONS ON A CYLINDRICAL CHANNEL

In a cylindrical pore, one can find analytical solutions for the exit pressure similar to the ones that Nazzal derived for the entry pressure. We derive here the corresponding expressions for the exit pressure in regimes 3 and 4, which correspond to equations (5) and (6). Note that these are approximate results that will match our model when the pore has a sharp transition at the edge $n \to \infty$.

Regime 3. The exit mechanism of the vesicle in this regime occurs when the top cap becomes perfectly flat ($\rho_1 = 0$) so the force balance can not be satisfied beyond this point. For a non-wetting vesicle and a cylindrical pore, this can only happen when z_1 is right at the edge of the cylinder (the curvature is constant within its walls). In that scenario, the vesicle is equivalent to a droplet in a flat surface and we can find our solution by equaling the original volume to a spherical cap resting on a flat surface:

$$V_0 = V_{cap} \tag{16}$$

$$\frac{4}{3}\pi R_0^3 = \frac{1}{3}\pi \frac{1}{\rho_2^3}(2 - 3\cos\theta + \cos^3\theta), \tag{17}$$

so we obtain $\rho_2^3 = (1-\cos\theta)(\sin^2\theta + 1 - \cos\theta)/4R_0^3$. The Laplace law in this particular case is simply $\Delta P^* = \rho_2$, and by introducing the value of the curvature we directly obtain equation (12).

Regime 4. This exit mechanism occurs when the contact angle approaches $\pi/2$ and the value of the curvature inside the cylinder tends to zero. In this situation, the force opposing the external pressure arises from the bottom cap and it will reach its maximum when its radius is minimum. In a cylindrical pore the minimal radius is equal to the pore radius s, and can only occur when the lower detachment point is exactly at the pore edge $z_2 = -b$ and $R_2 = s/\sin(\theta)$. The top cap is then inside the cylindrical channel and constrained by its walls, so its radius is simply $R_1 = s/\cos(\theta)$. By normalizing this quantities and introducing them into Laplace law we obtain the analytical expression for regime 4:

$$\Delta P^* = \cos\theta + \sin\theta. \tag{18}$$

[1] M. Cheryan, Membrane Technology , 5 (2005).
[2] J. Mueller, Y. Cen, and R. H. Davis, Journal of Membrane Science **129**, 221 (1997).
[3] H.-Y. Li, C. D. Bertram, and D. E. Wiley, AIChE Journal **44**, 1950 (1998).
[4] E. N. Tummons, V. V. Tarabara, J. W. Chew, and A. G. Fane, Journal of Membrane Science **500**, 211 (2015).
[5] K. Pantel, R. H. Brakenhoff, and B. Brandt, Nature reviews. Cancer **8**, 329 (2008).
[6] S. Stott, R. Lee, and S. Nagrath, Science Translational Medicine **2**, 25ra23 (2010).
[7] P. Xue, Y. Wu, J. Guo, and Y. Kang, Biomedical Microdevices **17** (2015), 10.1007/s10544-015-9945-x.
[8] T. A. Desai, D. J. Hansford, A. H. Nashat, G. Rasi, J. Tu, Y. Wang, M. Zhang, and M. Ferrari, Biomedical Microdevices **2**, 11 (2000).
[9] W. Beattie, X. Qin, L. Wang, and H. Ma, Lab on a Chip **14**, 2657 (2014).
[10] W. A. Lam, M. J. Rosenbluth, and D. A. Fletcher, British Journal of Haematology **142**, 497 (2008).
[11] H. Mohamed, M. Murray, J. N. Turner, and M. Caggana, Journal of Chromatography A **1216**, 8289 (2009).
[12] G. Hvichia, Z. Parveen, C. Wagner, M. Janning, J. Quidde, A. Stein, V. Müller, S. Loges, R. Neves, N. Stoecklein, H. Wikman, S. Riethdorf, K. Pantel, and T. Gorges, International Journal of Cancer **00**, n/a (2016).
[13] P. Preira, V. Grandné, J.-M. Forel, S. Gabriele, M. Camara, and O. Theodoly, Lab Chip **13**, 161 (2013).
[14] A. F. Sarioglu, N. Aceto, N. Kojic, M. C. Donaldson, M. Zeinali, B. Hamza, A. Engstrom, H. Zhu, T. K. Sundaresan, D. T. Miyamoto, X. Luo, A. Bardia, B. S. Wittner, S. Ramaswamy, T. Shioda, D. T. Ting, S. L. Stott, R. Kapur, S. Maheswaran, D. a. Haber, and M. Toner, Nature methods **12**, 1 (2015).
[15] S. M. McFaul, B. K. Lin, and H. Ma, Lab on a Chip **12**, 2369 (2012).
[16] R. D. Sochol, A. Lu, J. Lei, K. Iwai, L. P. Lee, and L. Lin, Lab on a chip **14**, 1585 (2014).
[17] E. Evans and a. Yeung, Biophysical journal **56**, 151 (1989).
[18] J. L. Drury and M. Dembo, Biophysical journal **76**, 110 (1999).
[19] J. Derganc, B. Bozic, S. Svetina, and B. Zeks, Biophysical journal **79**, 153 (2000).
[20] K. Akashi, H. Miyata, H. Itoh, and K. Kinosita, Biophysical journal **71**, 3242 (1996).
[21] X. Sun, W. D. Weinlandt, H. Patel, M. Wu, and C. J. Hernandez, Lab Chip **14**, 2491 (2014).
[22] F. F. Nazzal and M. R. Wiesner, Water Environment Research **68**, 1187 (1996).
[23] H. Bruus, "Theoretical microfluidics," (2008), arXiv:arXiv:1011.1669v3.
[24] F. Y. Leong, Q. Li, C. T. Lim, and K.-H. Chiam, Biomechanics and modeling in mechanobiology **10**, 755 (2011).
[25] Z. Zhang, J. Xu, B. Hong, and X. Chen, Lab on a chip **14**, 2576 (2014).
[26] D. Baratian, A. Cavalli, D. van den Ende, and F. Mugele, Soft Matter **13 Jul 201**, 7717 (2015).
[27] J.-B. Fournier and P. Galatola, Soft Matter **4**, 2463 (2008).
[28] E. Evans and W. Rawicz, Physical Review Letters **64**, 2094 (1990).
[29] K. Allen Rodowicz, H. Francisco, and B. Layton, Chemistry and Physics of Lipids **163**, 787 (2010).
[30] D. Needham and R. Hochmuth, Biophysical Journal **61**, 1664 (1992).
[31] U. Seifert, Zeitschrift für Physik B Condensed Matter **97**, 299 (1995).
[32] U. Seifert, Advances in Physics **46**, 13 (1997).
[33] W. Helfrich, Physical Review **39**, 5280 (1989).
[34] L. C. Foucard, J. Pellegrino, and F. J. Vernerey, Cmes-Computer Modeling in Engineering & Sciences **98**, 101 (2014).
[35] A. D. Petelska, Central European Journal of Chemistry **10**, 16 (2012).
[36] G. Khelashvili, B. Kollmitzer, P. Heftberger, G. Pabst, and D. Harries, Journal of Chemical Theory and Computation **9**, 3866 (2013).
[37] J. J. Kwan and M. A. Borden, Soft Matter **8**, 4756 (2012).
[38] E. Dressaire, R. Bee, D. C. Bell, A. Lips, and H. a. Stone, Science (New York, N.Y.) **320**, 1198 (2008).
[39] K. D. Girard, C. Chaney, M. Delannoy, S. C. Kuo, and D. N. Robinson, The EMBO journal **23**, 1536 (2004).
[40] D. V. Zhelev, D. Needham, and R. M. Hochmuth, Biophysical journal **67**, 696 (1994).
[41] P.-G. de Gennes, F. Brochard-Wyart, and D. Quere, *Capillarity and Wetting Phenomena* (Springer New York, 2004) p. 291.
[42] P. Renvoisé, J. W. M. Bush, M. Prakash, and D. Quéré, EPL (Europhysics Letters) **86**, 64003 (2009).
[43] L. C. Foucard and F. J. Vernerey, International Journal for Numerical Methods in Engineering **107**, 923 (2016).
[44] S. Kosvintsev, P. Sutrisna, I. Cumming, R. Holdich, and G. Mason, Chemical Engineering Research and Design **85**, 530 (2007).
[45] N. Champagne, R. Vasseur, A. Montourcy, and D. Bartolo, Physical Review Letters **105**, 2 (2010), arXiv:1005.5003.
[46] M. Szwast, T. Suchecka, and W. Piatkiewicz, Chemical and Process Engineering - Inzynieria Chemiczna i Procesowa **33**, 385 (2012).
[47] C. Dekker, Nature nanotechnology **2**, 209 (2007).
[48] R. M. Hochmuth, Journal of Biomechanics **33**, 15 (2000).
[49] D. G. Hunter and B. J. Frisken, Biophysical journal **74**, 2996 (1998).
[50] T. Darvishzadeh and N. V. Priezjev, Journal of Membrane Science **423-424**, 468 (2012), arXiv:arXiv:1208.5668v1.
[51] L. Gorre, E. Ioannidis, and P. Silberzan, Europhysics Letters (EPL) **33**, 267 (1996).
[52] Q. Guo, S. M. McFaul, and H. Ma, Physical Review E - Statistical, Nonlinear, and Soft Matter Physics **83**, 1 (2011).
[53] T. F. Headen, S. M. Clarke, A. Perdigon, G. H. Meeten, J. D. Sherwood, and M. Aston, Journal of Colloid and Interface Science **304**, 562 (2006).
[54] J. R. Henriksen and J. H. Ipsen, European Physical Journal E **14**, 149 (2004).
[55] W. D. Merryman, I. Youn, H. D. Lukoff, P. M. Krueger, F. Guilak, R. A. Hopkins, and M. S. Sacks, American journal of physiology. Heart and circulatory physiology

290, H224 (2006).
[56] D. C. Leslie, C. J. Easley, E. Seker, J. M. Karlinsey, M. Utz, M. R. Begley, and J. P. Landers, Nature Physics **5**, 231 (2009).
[57] B. Mosadegh, C.-H. Kuo, Y.-C. Tung, Y.-s. Torisawa, T. Bersano-Begey, H. Tavana, and S. Takayama, Nature Physics **6**, 433 (2010).